

Tropical Cyclone Boundary Layer Shocks

CHRISTOPHER J. SLOCUM *

Department of Atmospheric Science, Colorado State University, Fort Collins, Colorado, USA

GABRIEL J. WILLIAMS

Department of Physics and Astronomy, College of Charleston, Charleston, South Carolina, USA

RICHARD K. TAFT AND WAYNE H. SCHUBERT

Department of Atmospheric Science, Colorado State University, Fort Collins, Colorado, USA

ABSTRACT

This paper presents numerical solutions and idealized analytical solutions of axisymmetric, f -plane models of the tropical cyclone boundary layer. In the numerical model, the boundary layer radial and tangential flow is forced by a specified pressure field, which can also be interpreted as a specified gradient balanced tangential wind field $v_{gr}(r)$ or vorticity field $\zeta_{gr}(r)$. When the specified $\zeta_{gr}(r)$ field is changed from one that is radially concentrated in the inner core to one that is radially spread, the quasi-steady-state boundary layer flow transitions from a single eyewall shock-like structure to a double eyewall shock-like structure. To better understand these structures, analytical solutions are presented for two simplified versions of the model. In the simplified analytical models, which do not include horizontal diffusion, the $u(\partial u/\partial r)$ term in the radial equation of motion and the $u[f + (\partial v/\partial r) + (v/r)]$ term in the tangential equation of motion produce discontinuities in the radial and tangential wind, with associated singularities in the boundary layer pumping and the boundary layer vorticity. In the numerical model, which does include horizontal diffusion, the radial and tangential wind structures are not true discontinuities, but are shock-like, with wind changes of 20 or 30 m s⁻¹ over a radial distance of a few kilometers. When double shocks form, the outer shock can control the strength of the inner shock, an effect that likely plays an important role in concentric eyewall cycles.

1. Introduction

Williams et al. (2013) interpreted the structure of the boundary layer wind field in Hurricane Hugo (1989) in terms of an axisymmetric slab boundary layer model. They explained Hugo's 20 m s⁻¹ eyewall vertical velocity at 450 m height by dry dynamics, i.e., by the formation of a shock-like structure in the boundary layer radial inflow, with small radial flow on the inside edge and large radial inflow

on the outside edge of the structure. Such features appear to be primarily a phenomenon of the boundary layer because the radial flow is an order of magnitude larger in the boundary layer compared to the overlying fluid (typically 20 m s⁻¹ versus 2 m s⁻¹). Large inflow in the boundary layer also leads to large tangential wind tendencies, resulting in a shock-like structure in the boundary layer tangential wind. Since the radial derivative of the radial velocity is related to the boundary layer pumping, and the radial derivative of the tangential velocity is related to the vertical component of relative vorticity, a thin annulus of very large boundary layer pumping and very high vorticity

* *Corresponding author address:* Christopher J. Slocum,
Department of Atmospheric Science, Colorado State University,
Fort Collins, Colorado, USA.
E-mail: cslocum@atmos.colostate.edu

develops as part of the shock structure.

The purpose of the present paper is to add analytical support to the arguments of Williams et al. (2013) and to extend their work to the concentric eyewall case. The theoretical basis for the present arguments is again the axisymmetric, primitive equation version of the slab boundary layer model. The interpretation is again in terms of Burgers' shock effects, for which an excellent general mathematical discussion can be found in the book by Whitham (1974).

The paper is organized in the following way. Section 2 gives a brief review of the slab boundary layer model that was described in detail by Williams et al. (2013). In order to gain a semi-quantitative understanding of the solutions to the slab boundary layer equations, sections 3 and 4 present some analytical solutions of simplified versions of the model. These solutions illustrate the formation of discontinuities in the radial and tangential winds, and thus the formation of singularities in the boundary layer pumping and the boundary layer vorticity. One application of these analytical solutions is to the formation of concentric eyewalls, which is discussed in section 5. Numerical solutions of the complete nonlinear model are presented in section 6. In the numerical model, horizontal diffusion terms are used to maintain single-valued solutions, so that the numerically modeled structures are "shock-like" rather than true "shocks", although for convenience we shall use these terms somewhat interchangeably. The numerical solutions are used to better understand the role of an outer eyewall shock in controlling the structure of an inner eyewall shock. Section 7 presents some concluding remarks, including the implications of the present work on understanding eyewall replacement cycles.

2. Slab Boundary Layer Model

The model considers axisymmetric, boundary layer motions of an incompressible fluid on an f -plane. The frictional boundary layer is assumed to have constant depth h , with radial and azimuthal velocities $u(r, t)$ and $v(r, t)$ that are independent of height between the top of a thin surface layer and height h , and with vertical velocity $w(r, t)$ at height h . In the overlying layer the radial velocity is assumed to be negligible and the azimuthal velocity $v_{\text{gr}}(r, t)$ is assumed to be in gradient balance and to be a specified function of radius and time. The boundary layer flow is driven by the same radial pressure gradient force that occurs in the overlying fluid, so that, in the radial equation of boundary layer motion, the pressure gradient force can be expressed as the specified function $[f + (v_{\text{gr}}/r)]v_{\text{gr}}$. The governing system of differential equations for the boundary layer variables $u(r, t)$, $v(r, t)$, and $w(r, t)$ then takes

the form

$$\frac{\partial u}{\partial t} + u \frac{\partial u}{\partial r} + w^- \left(\frac{u}{h} \right) = \left(f + \frac{v + v_{\text{gr}}}{r} \right) (v - v_{\text{gr}}) - c_D U \frac{u}{h} + K \frac{\partial}{\partial r} \left(\frac{\partial(ru)}{r \partial r} \right), \quad (1)$$

$$\frac{\partial v}{\partial t} + u \left(f + \frac{\partial v}{\partial r} + \frac{v}{r} \right) + w^- \left(\frac{v - v_{\text{gr}}}{h} \right) = -c_D U \frac{v}{h} + K \frac{\partial}{\partial r} \left(\frac{\partial(rv)}{r \partial r} \right), \quad (2)$$

$$w = -h \frac{\partial(ru)}{r \partial r} \quad \text{and} \quad w^- = \frac{1}{2}(|w| - w), \quad (3)$$

where

$$U = 0.78 (u^2 + v^2)^{1/2} \quad (4)$$

is the wind speed at 10 m height, f the constant Coriolis parameter, and K the constant horizontal diffusivity. The drag coefficient c_D is assumed to depend on the 10 m wind speed according to

$$c_D = 10^{-3} \begin{cases} 2.70/U + 0.142 + 0.0764U & \text{if } U \leq 25 \\ 2.16 + 0.5406 \{1 - \exp[-(U - 25)/7.5]\} & \text{if } U \geq 25, \end{cases} \quad (5)$$

where the 10 m wind speed U is expressed in m s^{-1} . The boundary conditions are

$$\left. \begin{array}{l} u = 0 \\ v = 0 \end{array} \right\} \text{ at } r = 0, \quad \left. \begin{array}{l} \frac{\partial(ru)}{\partial r} = 0 \\ \frac{\partial(rv)}{\partial r} = 0 \end{array} \right\} \text{ at } r = b, \quad (6)$$

where b is the radius of the outer boundary. The initial conditions are

$$u(r, 0) = u_0(r) \quad \text{and} \quad v(r, 0) = v_0(r), \quad (7)$$

where $u_0(r)$ and $v_0(r)$ are specified functions. The forcing $v_{\text{gr}}(r, t)$ is discussed in section 6.

Applications of the slab boundary layer model (1)–(7), or closely related models, have a rich history in the literature of hurricane dynamics. For at least a partial appreciation of this history, the reader is referred to the analyses and numerical simulations found in Ooyama (1969a,b), Chow (1971), Shapiro (1983), Emanuel (1986, 1989), Kepert and Wang (2001), Kepert (2001, 2010a,b, 2013), Smith (2003), Smith and Vogl (2008), Smith et al. (2008, 2009), Smith and Montgomery (2008, 2010), Smith and Thomsen (2010), Slocum (2013), and Abarca and Montgomery (2013). As in the work of Williams et al. (2013), our emphasis here is on high resolution simulations that capture the shock formation process.

In the absence of the horizontal diffusion terms, the slab boundary layer equations constitute a hyperbolic system that can be written in characteristic form (see the Appendix). A knowledge of the characteristic form is useful in understanding the formation of shocks. In fact, before presenting numerical solutions of the system (1)–(7) in section 6, we next discuss some analytical solutions of two simplified versions of the model, i.e., two versions that have very simple characteristic forms. These analytical solutions aid in understanding the formation of discontinuities in the radial and tangential flow, and hence singularities in the vertical velocity and vorticity.

3. Analytical Model I

The formation of shocks in the u and v fields in the hurricane boundary layer depends on the $u(\partial u/\partial r)$ and $u[f + (\partial v/\partial r) + (v/r)]$ terms in (1) and (2), with the term proportional to the agradient tangential flow $(v - v_{\text{gr}})$ serving as a forcing mechanism for $(\partial u/\partial t)$, the surface friction terms serving to damp u and v , and the horizontal diffusion terms serving to control the structure near the shock. As we shall see, the shocks in u and v occur at the same time and at the same radius. These discontinuities in the radial and tangential flow mean that there is a circle of infinite vertical velocity at the top of the boundary layer and a circular infinite vorticity sheet in the boundary layer.

To obtain a semi-quantitative understanding of the above concepts, we now approximate (1) and (2) by neglecting the horizontal diffusion terms, the w^- terms, the surface drag terms, and the $(v - v_{\text{gr}})$ forcing term. The radial and tangential momentum equations (1) and (2) then simplify to

$$\frac{\partial u}{\partial t} + u \frac{\partial u}{\partial r} = 0, \quad (8)$$

$$\frac{\partial v}{\partial t} + u \left(f + \frac{\partial v}{\partial r} + \frac{v}{r} \right) = 0. \quad (9)$$

Although the simplified equations (8) and (9) cannot be justified through a rigorous scale analysis of tropical cyclone boundary layer dynamics, they do contain an important part of the dynamics involved in boundary layer shocks. However, it should be noted that there is an important conceptual difference between the simple analytical model equations (8) and (9) and the original model equations (1) and (2). When we present numerical solutions of (1) and (2) in section 6, the initial condition will have no radial flow, so that a shock-like structure in u will develop only after u has been forced through the $[f + (v + v_{\text{gr}})/r](v - v_{\text{gr}})$ term in (1). In contrast, the analytical solutions presented here will develop, not from this forcing effect, but rather from a nonzero initial condition on u .

The solutions of (8) and (9) are easily obtained by noting

that these two equations can be written in the form

$$\frac{du}{dt} = 0, \quad (10)$$

$$\frac{d(rv + \frac{1}{2}fr^2)}{dt} = 0, \quad (11)$$

where $(d/dt) = (\partial/\partial t) + u(\partial/\partial r)$ is the derivative following the boundary layer radial motion. According to (10) and (11), the radial velocity u and the absolute angular momentum $rv + \frac{1}{2}fr^2$ are the Riemann invariants for analytical model I. Integration of (10) and (11), with use of the initial conditions (7), yields the solutions

$$u(r, t) = u_0(\hat{r}), \quad (12)$$

$$v(r, t) = \left(v_0(\hat{r}) + \frac{1}{2}f\hat{r} \right) \frac{\hat{r}}{r} - \frac{1}{2}fr, \quad (13)$$

where the characteristics $\hat{r}(r, t)$ are given implicitly by

$$r = \hat{r} + tu_0(\hat{r}), \quad (14)$$

which is easily obtained by integration of $(dr/dt) = u$, with u given by (12). For a given \hat{r} , (14) defines a straight characteristic in (r, t) , along which the radial velocity $u(r, t)$ is fixed according to (12), and along which the absolute angular momentum $rv(r, t) + \frac{1}{2}fr^2$ is fixed according to (13).

To understand when the derivatives $(\partial u/\partial r)$ and $(\partial v/\partial r)$ become infinite, and to also check that (12), (13), and (14) constitute solutions of (8) and (9), we first note that $(\partial/\partial t)$ and $(\partial/\partial r)$ of (14) yield

$$\begin{aligned} -\frac{\partial \hat{r}}{\partial t} &= \frac{u_0(\hat{r})}{1 + tu'_0(\hat{r})}, \\ \frac{\partial \hat{r}}{\partial r} &= \frac{1}{1 + tu'_0(\hat{r})}, \end{aligned} \quad (15)$$

so that $(\partial/\partial t)$ and $u(\partial/\partial r)$ of (12) yield

$$\begin{aligned} \frac{\partial u}{\partial t} &= u'_0(\hat{r}) \frac{\partial \hat{r}}{\partial t} = -\frac{u_0(\hat{r})u'_0(\hat{r})}{1 + tu'_0(\hat{r})}, \\ u \frac{\partial u}{\partial r} &= u_0(\hat{r})u'_0(\hat{r}) \frac{\partial \hat{r}}{\partial r} = \frac{u_0(\hat{r})u'_0(\hat{r})}{1 + tu'_0(\hat{r})}, \end{aligned} \quad (16)$$

where the final equalities in (16) follow from using (15) to eliminate $(\partial \hat{r}/\partial t)$ and $(\partial \hat{r}/\partial r)$. The sum of the two lines in (16) then confirms that (12) and (14) constitute a solution of (8). A similar argument confirms that (13) and (14) constitute a solution of (9). However, it should be noted that these solutions may be multivalued, in which case (12)–(14) must be amended in such a way as to guarantee the solutions are single valued. In other words, after the shock formation time t_s , a shock-tracking procedure is required. To compute t_s we note that, from the denominators on the right-hand sides of (16), the derivatives $(\partial u/\partial t)$ and $(\partial u/\partial r)$ become infinite when

$$tu'_0(\hat{r}) = -1 \quad (17)$$

along one or more of the characteristics. For a typical tropical cyclone, the initial radial velocity profile $u_0(r)$ is such that its derivative $u'_0(r)$ is both positive (for larger r) and negative (for smaller r). Let \hat{r}_s denote the characteristic that originates at the minimum value of $u'_0(r)$, i.e., $u'_0(\hat{r}_s) = [u'_0(r)]_{\min}$. Note that $u'_0(\hat{r}_s)$ will be the most negative value of $u'_0(\hat{r})$ and will satisfy (17) at the earliest time. Therefore, the time of shock formation, determined from (17), is

$$t_s = -\frac{1}{u'_0(\hat{r}_s)}, \quad (18)$$

and the radius of shock formation, determined from (14) and (18), is

$$r_s = \hat{r}_s - \frac{u_0(\hat{r}_s)}{u'_0(\hat{r}_s)}. \quad (19)$$

For typical tropical cyclone cases, $u_0(\hat{r}_s) < 0$ and $u'_0(\hat{r}_s) < 0$, so the shock forms a distance $u_0(\hat{r}_s)/u'_0(\hat{r}_s)$ inside \hat{r}_s .

From the solutions (12) and (13) we can compute the solutions for the divergence $\delta(r, t) = \partial[ru(r, t)]/r\partial r$ and the relative vorticity $\zeta(r, t) = \partial[rv(r, t)]/r\partial r$. The relative vorticity is obtained by differentiation of (13), which yields

$$\zeta(r, t) = \left(\frac{f + \zeta_0(\hat{r})}{1 + tu'_0(\hat{r})} \right) \frac{\hat{r}}{r} - f, \quad (20)$$

where $\zeta_0(r) = \partial[rv_0(r)]/r\partial r$ is the initial relative vorticity. Similarly, the boundary layer divergence $\delta(r, t)$, or equivalently the boundary layer pumping $w(r, t) = -h\delta(r, t)$, is obtained by using (12) in (3), which yields

$$w(r, t) = -h \left(\frac{u'_0(\hat{r})}{1 + tu'_0(\hat{r})} + \frac{u_0(\hat{r})}{r} \right). \quad (21)$$

Because of the factors $1 + tu'_0(\hat{r})$ in the denominators of (20) and (21), the relative vorticity $\zeta(r, t)$ and the boundary layer pumping $w(r, t)$ become infinite at the same time ($t = t_s$) and the same place ($r = r_s$).

As a simple example, consider the initial conditions

$$u_0(r) = u_m \left(\frac{4(r/a)^3}{1 + 3(r/a)^4} \right), \quad (22)$$

$$v_0(r) = v_m \left(\frac{2(r/a)}{1 + (r/a)^2} \right), \quad (23)$$

where the constants a , u_m , and v_m specify the radial extent and strength of the initial radial and tangential flow. The derivative of (22) is

$$u'_0(r) = \frac{12u_m}{a} \left(\frac{(r/a)^2[1 - (r/a)^4]}{[1 + 3(r/a)^4]^2} \right), \quad (24)$$

while the initial relative vorticity, obtained by differentiation of (23), is

$$\zeta_0(r) = \frac{4v_m}{a[1 + (r/a)^2]^2}. \quad (25)$$

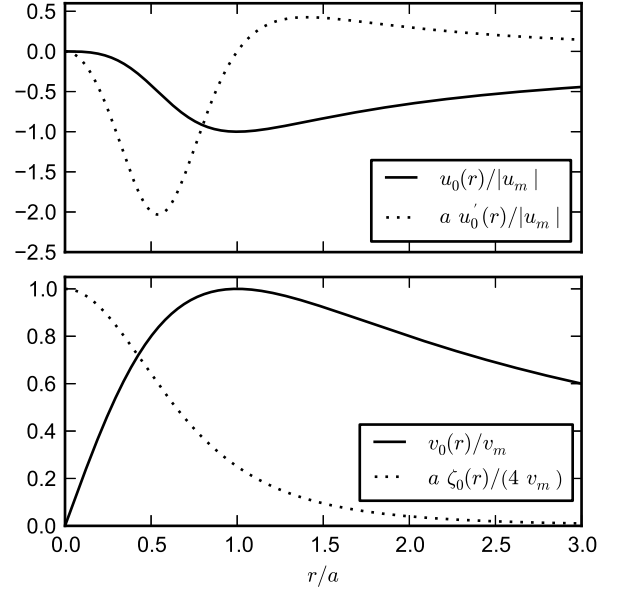


FIG. 1. The dimensionless initial conditions used in the analytical models for the single eyewall cases as computed from equations (22)–(25). The solid line in the upper panel shows the dimensionless initial radial velocity $u_0(r)/|u_m|$ for the case in which $u_m < 0$, while the dotted line shows its dimensionless radial derivative $a u'_0(r)/|u_m|$. Similarly, the solid line in the lower panel shows the dimensionless initial tangential velocity $v_0(r)/v_m$, while the dotted line shows the dimensionless initial vorticity $a \zeta_0(r)/(4v_m)$.

The dimensionless forms of the initial profiles (22)–(25) are plotted in Figure 1. Note that $u'_0(r) = 0$ at $r = 0$ and $r = a$. For this example, the minimum value of $u'_0(\hat{r})$ occurs at $\hat{r} = \hat{r}_s$, where

$$\hat{r}_s = \left(2 - \frac{\sqrt{33}}{3} \right)^{1/4} a \approx 0.5402 a, \quad (26)$$

so that, from (24),

$$u'_0(\hat{r}_s) \approx 2.032 \frac{u_m}{a}. \quad (27)$$

From (18), the time of shock formation is

$$t_s \approx -\frac{a}{2.032 u_m}, \quad (28)$$

and, from (19), the radius of shock formation is

$$r_s \approx 0.5426 \hat{r}_s \approx 0.2931 a. \quad (29)$$

Table 1 lists values of t_s and r_s obtained from model I for seven different single eyewall test cases (S1 through S7) ranging from very weak vortices to hurricane strength vortices. For hurricane strength vortices, the shock formation

TABLE 1. Test Cases and Results for Analytical Models I and II

Test Case	Parameters Defining Initial Conditions			Typical Values Needed in Model II		Shock Results From Models I and II			
	a (km)	u_m (m s ⁻¹)	v_m (m s ⁻¹)	U (m s ⁻¹)	τ (h)	Shock	r_s (km)	$t_s^{(I)}$ (h)	$t_s^{(II)}$ (h)
S1	300	-0.5	3.2	2.5	78.6	Single	87.9	82.0	No Shock
S2	200	-1.0	6.3	5.0	52.2	Single	58.6	27.3	38.7
S3	150	-2.0	12.7	10.0	23.6	Single	44.0	10.2	13.4
S4	100	-4.0	25.3	20.0	7.69	Single	29.3	3.42	4.52
S5	60	-6.0	38.0	30.0	3.82	Single	17.6	1.37	1.69
S6	40	-8.0	50.7	40.0	2.64	Single	11.7	0.684	0.791
S7	30	-10.0	63.3	50.0	2.07	Single	8.79	0.410	0.457
D1	60	-6.0	38.0	30.0	3.82	Inner	17.6	1.37	1.69
						Outer	29.6	2.43	3.85

time is generally less than 1 hour. These rapid shock formation times for strong vortices indicate that, if disrupted, hurricane eyewalls can rapidly reform.

For the initial conditions given by (22) and (23), the solutions (12) and (13) take the form

$$u(r, t) = u_m \left(\frac{4(\hat{r}/a)^3}{1 + 3(\hat{r}/a)^4} \right), \quad (30)$$

$$v(r, t) = \left(\frac{2v_m(\hat{r}/a)}{1 + (\hat{r}/a)^2} + \frac{1}{2}f\hat{r} \right) \frac{\hat{r}}{r} - \frac{1}{2}fr, \quad (31)$$

where the characteristic curves (along which \hat{r} is fixed) are defined by

$$r = \hat{r} + u_m t \left(\frac{4(\hat{r}/a)^3}{1 + 3(\hat{r}/a)^4} \right). \quad (32)$$

Using (20), the relative vorticity takes the form

$$\zeta(r, t) = \left(f + \frac{4v_m}{a[1 + (\hat{r}/a)^2]^2} \right) \left(\frac{(\hat{r}/r)}{1 + tu'_0(\hat{r})} \right) - f, \quad (33)$$

while, using (21), the boundary layer pumping takes the form

$$w(r, t) = - \left(\frac{4hu_m(\hat{r}/a)^2}{a[1 + 3(\hat{r}/a)^4]} \right) \left(\frac{3[1 - (\hat{r}/a)^4]}{[1 + tu'_0(\hat{r})][1 + 3(\hat{r}/a)^4]} + \frac{\hat{r}}{r} \right). \quad (34)$$

The solutions for $u(r, t)$, $v(r, t)$, $\hat{r}(r, t)$, as given by (30)–(32), are plotted in the two panels of Figure 2 for the particular constants given in Table 1 for single eyewall test

case S5 (i.e., $a = 60$ km, $u_m = -6$ m s⁻¹, $v_m = 38$ m s⁻¹). The plots cover the radial interval $0 \leq r \leq 100$ km and the time interval $0 \leq t \leq t_s$, where $t_s = 1.37$ h is the shock formation time for this particular initial condition. Another view of this analytical solution is given in Figure 3, with the four panels displaying the radial profiles (at $t = 0$ in blue and at $t = t_s$ in red) of u, v, w, ζ . Also shown by the black curves in the top two panels are fluid particle displacements for particles that are equally spaced at the initial time. At $t = t_s$ the u and v fields become discontinuous at $r = 17.6$ km, while the w and ζ fields become singular there.

The solutions plotted in Figure 2 cover the time interval $0 \leq t \leq t_s$. How can we extend the solutions beyond $t = t_s$, i.e., into a region of the (r, t) -plane where characteristics intersect and (30)–(32) yield multivalued solutions? One obvious way to address this issue is to return to the model equations (8)–(9) and include horizontal diffusion terms. Indeed, this is the approach that will control the shock-like structures in the numerical solutions of section 6. However, even in the absence of horizontal diffusion terms, we can amend the analytical solutions to guarantee they are single-valued. One procedure is as follows. Let $R(t)$ denote the shock radius at time t , where $t \geq t_s$. Let $\hat{r}_1(t)$ denote the label of the characteristic that just touches the inside edge of the shock at time t , and $\hat{r}_2(t)$ denote the label of the characteristic that just touches the outside edge of the shock at time t . Then, from (14), we obtain

$$\begin{aligned} R(t) &= \hat{r}_1(t) + tu_0(\hat{r}_1(t)), \\ R(t) &= \hat{r}_2(t) + tu_0(\hat{r}_2(t)), \end{aligned} \quad (35)$$

which respectively determine $\hat{r}_1(t)$ and $\hat{r}_2(t)$ from a given

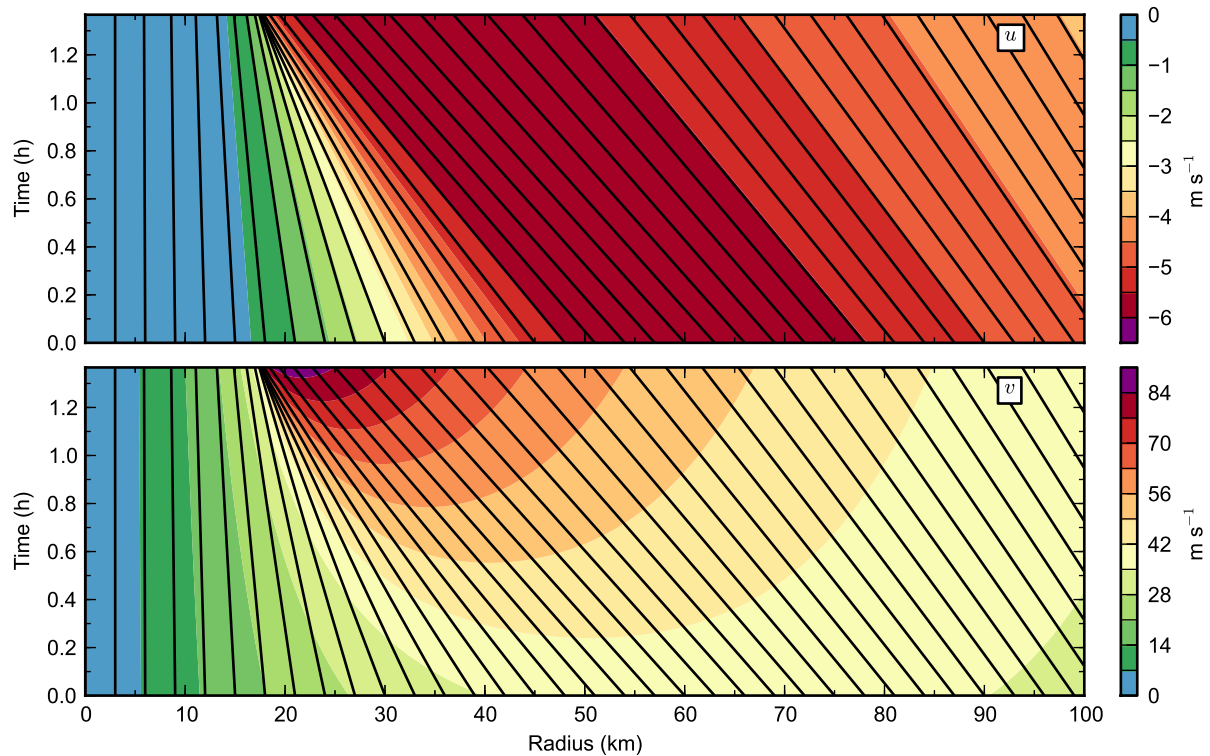


FIG. 2. The analytical solutions $u(r, t)$ and $v(r, t)$ from model I (color contours), as well as the characteristic curves (black lines on each panel), for the single eyewall case. These solutions are for the particular initial conditions (22) and (23), with the parameters given in Table 1 for test case S5 (i.e., $a = 60$ km, $u_m = -6$ m s $^{-1}$, $v_m = 38$ m s $^{-1}$). The plots cover the time interval $0 \leq t \leq t_s$, where $t_s = 1.37$ h is the shock formation time for this particular initial condition.

$R(t)$. The last equation needed to track the shock is an appropriate jump condition across the shock, which yields a first order ordinary differential equation relating $dR(t)/dt$ to $\hat{r}_1(t)$ and $\hat{r}_2(t)$. Without going into the details of such arguments (see Whitham (1974) for further discussion), we simply note that the solution of this ordinary differential equation for $R(t)$, along with (35), yields the three functions $R(t)$, $\hat{r}_1(t)$, $\hat{r}_2(t)$. This constitutes a shock-tracking procedure. We shall not further explore this procedure, but rather simply note that such shock-tracking procedures would probably never be used in three-dimensional, full-physics hurricane models because they become very complicated in more than one spatial dimension and when shocks can intersect. For a numerical model, a practical alternative to a shock-tracking procedure is a shock-capturing procedure, i.e., a procedure that captures the shock in a single grid volume for finite volume methods, or equivalently, between two grid points for finite difference methods. Shock capturing is a fundamental part of certain finite volume and finite difference methods based on the adaptive discretization concepts used in the essentially non-oscillatory (ENO) and the weighted essentially non-oscillatory (WENO) schemes (see the text by Durran

(2010) and the review by Shu (1998)). Shock capturing is also part of the finite volume methods used in the software package CLAWPACK, which is described by LeVeque (2002). With certain user-supplied routines, this software package is capable of solving the nonlinear system (1)–(7) without the horizontal diffusion terms. An advantage of using these shock-capturing methods is that they can reduce both smearing and nonphysical oscillations near the discontinuity. Although the numerical solutions of section 6 do not make use of shock capturing methods, these are interesting alternatives to the simple methods used here.

For the single eyewall case shown in Figures 2 and 3 the minimum value of $u'_0(r)$ occurs at $r \approx 32.4$ km, and the shock forms at $r \approx 17.6$ km. In another class of initial conditions (not explored here) the minimum value of $u'_0(r)$ occurs at $r = 0$, in which case the shock forms at the center of the vortex. Although such initial conditions are probably less relevant, they may explain certain features in simulated and real hurricanes, e.g., the very small “vortex-within-a-vortex” sometimes seen in axisymmetric model simulations (Yamasaki (1983), his Figures 18 and 20; Hausman et al. (2006), their Figures 3 and 6) and the hub cloud sometimes seen in real hurricanes (Schubert et al. 2007).

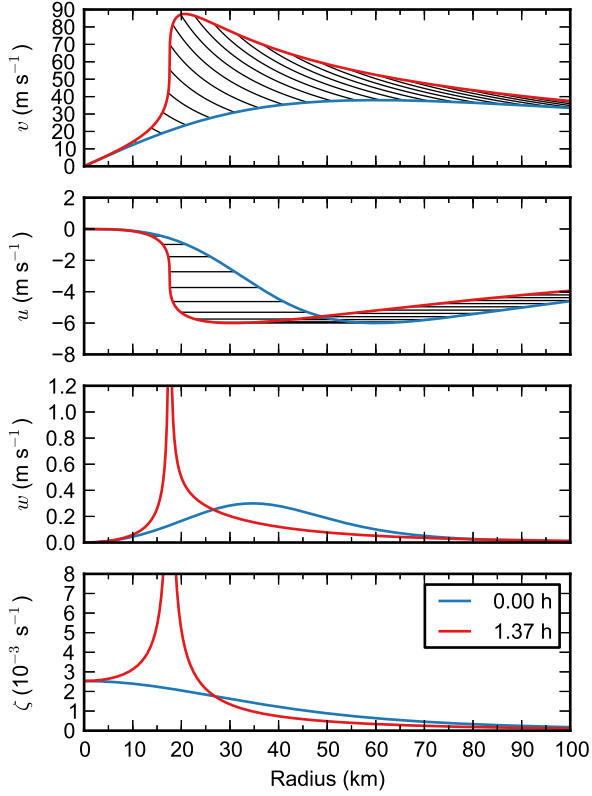


FIG. 3. The radial profiles of v, u, w, ζ at $t = 0$ (blue) and at $t = t_s = 1.37$ h (red) for analytical model I and single eyewall test case S5. Also shown by the black curves in the top two panels are fluid particle displacements for particles that are equally spaced at the initial time. At $t = t_s$ the u and v fields become discontinuous at $r = r_s = 17.6$ km, while the w and ζ fields become singular there.

4. Analytical Model II

We now consider a second analytical model that adds surface drag effects to the model considered in section 3. For simplicity, we linearize the surface drag terms so the radial and tangential momentum equations become

$$\frac{\partial u}{\partial t} + u \frac{\partial u}{\partial r} = -\frac{u}{\tau}, \quad (36)$$

$$\frac{\partial v}{\partial t} + u \left(f + \frac{\partial v}{\partial r} + \frac{v}{r} \right) = -\frac{v}{\tau}, \quad (37)$$

where the constant damping time scale τ is a typical value of $h/(c_D U)$. The values of τ used for the test cases defined in Table 1 are given in the sixth column of that table and were computed using $h = 1000$ m, c_D as given in (5), and the values of U given in the fifth column of Table 1. These typical values of U were computed by finding the maximum value of U for the initial vortex of each test case.

The solutions of (36) and (37) are easily obtained by noting that these two equations can be written in the form

$$\frac{d}{dt} \left\{ u e^{t/\tau} \right\} = 0, \quad (38)$$

$$\frac{d}{dt} \left\{ r v e^{t/\tau} + f [\hat{r} t + u_0(\hat{r}) \tau (t - \hat{t})] u_0(\hat{r}) \right\} = 0, \quad (39)$$

where $(d/dt) = (\partial/\partial t) + u(\partial/\partial r)$ is again defined as the derivative following the boundary layer radial motion, and where the characteristics $\hat{r}(r, t)$ are given implicitly by

$$r = \hat{r} + \hat{t} u_0(\hat{r}), \quad (40)$$

with the function $\hat{t}(t)$ defined by

$$\hat{t} = \tau (1 - e^{-t/\tau}). \quad (41)$$

The quantities within the braces in (38) and (39) are the Riemann invariants for analytical model II. The equivalence of (37) and (39) is easily checked by converting (39) to (37) through the use of $\tau [d(t - \hat{t})/dt] = \hat{t}$, followed by the use of (40).

Integration of (38) and (39), with use of the initial conditions (7), yields the solutions

$$u(r, t) = u_0(\hat{r}) e^{-t/\tau}, \quad (42)$$

$$r v(r, t) = \left\{ \hat{r} v_0(\hat{r}) - f [\hat{r} t + u_0(\hat{r}) \tau (t - \hat{t})] u_0(\hat{r}) \right\} e^{-t/\tau}. \quad (43)$$

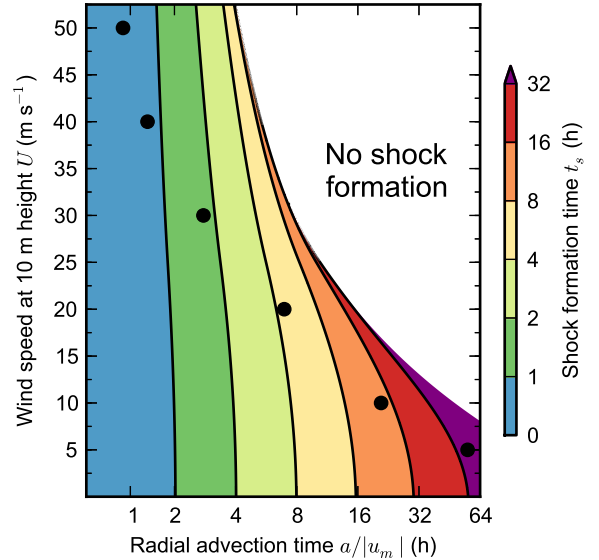


FIG. 4. Isolines of the shock formation time t_s (with color scale at right) computed from (52) as a function of the radial advection time $a/|u_m|$ and the 10 m wind speed U . The six dots correspond to the parameters given in Table 1 for the single eyewall test cases S2 through S7.

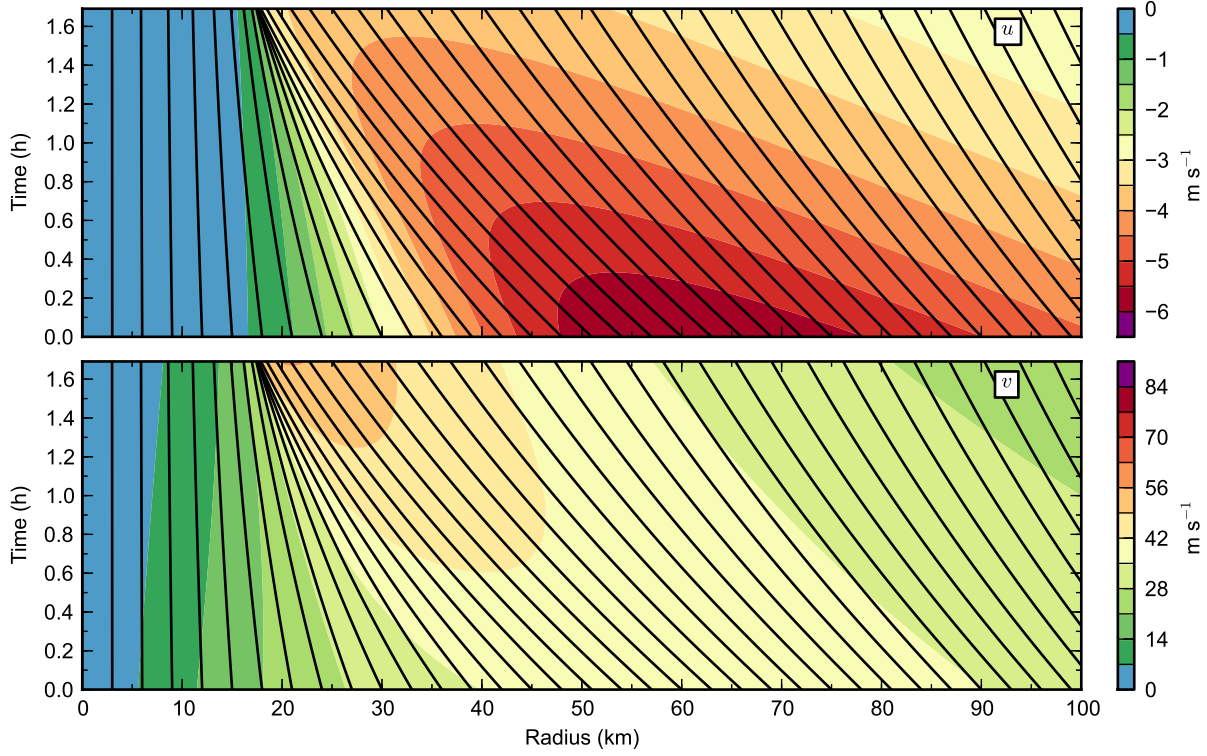


FIG. 5. The analytical solutions $u(r, t)$ and $v(r, t)$ from model II (color contours), as well as the characteristic curves (black curves on each panel), for the single eyewall case. These solutions are for the particular initial conditions (22) and (23), with the parameters given in Table 1 for test case S5 (i.e., $a = 60$ km, $u_m = -6$ m s $^{-1}$, $v_m = 38$ m s $^{-1}$). The plots cover the time interval $0 \leq t \leq t_s$, where $t_s = 1.69$ h is the shock formation time for model II with this particular initial condition.

As in section 3, (40) is easily obtained by integration of $(dr/dt) = u$, but with u now given by (42). For a given \hat{r} , (40) defines a curved characteristic in (r, t) , along which $u(r, t)$ exponentially damps according to (42), and along which, according to (43), $v(r, t)$ varies in a more complicated way that includes the factor $(\hat{r}/r)e^{-t/\tau}$. Along a given characteristic, the behavior of $u(r, t)$ can be quite different from the behavior of $v(r, t)$ because the effect of the (\hat{r}/r) amplification factor can more than compensate the $e^{-t/\tau}$ damping factor and cause $v(r, t)$ to increase along some characteristics.

Another useful representation of the solution (43) is obtained by using (40) to eliminate $u_0(\hat{r})$, yielding the form

$$rv(r, t) = \left\{ \hat{r}v_0(\hat{r}) + f \frac{t}{\hat{t}} \left[\hat{r} + (r - \hat{r}) \left(\frac{\tau(t - \hat{t})}{t\hat{t}} \right) \right] (\hat{r} - r) \right\} e^{-t/\tau}, \quad (44)$$

which is analogous to the frictionless form (13). In fact, for $(t/\tau) \ll 1$, it can be shown that $(t/\hat{t}) \approx 1$ and $\tau(t - \hat{t})/(t\hat{t}) \approx 1/2$, in which case (44) reduces to (13).

To understand when the derivatives $(\partial u/\partial r)$ and $(\partial v/\partial r)$ become infinite, we first note that $(\partial/\partial t)$ and $(\partial/\partial r)$ of (40) yield

$$\begin{aligned} -\frac{\partial \hat{r}}{\partial t} &= \frac{u_0(\hat{r})e^{-t/\tau}}{1 + \hat{t}u'_0(\hat{r})}, \\ \frac{\partial \hat{r}}{\partial r} &= \frac{1}{1 + \hat{t}u'_0(\hat{r})}, \end{aligned} \quad (45)$$

so that $(\partial/\partial t + 1/\tau)$ and $u(\partial/\partial r)$ of (42) yield

$$\begin{aligned} \frac{\partial u}{\partial t} + \frac{u}{\tau} &= e^{-t/\tau} u'_0(\hat{r}) \frac{\partial \hat{r}}{\partial t} = -\frac{e^{-2t/\tau} u_0(\hat{r}) u'_0(\hat{r})}{1 + \hat{t}u'_0(\hat{r})}, \\ u \frac{\partial u}{\partial r} &= e^{-2t/\tau} u_0(\hat{r}) u'_0(\hat{r}) \frac{\partial \hat{r}}{\partial r} = \frac{e^{-2t/\tau} u_0(\hat{r}) u'_0(\hat{r})}{1 + \hat{t}u'_0(\hat{r})}, \end{aligned} \quad (46)$$

where the final equalities in (46) follow from using (45) to eliminate $(\partial \hat{r}/\partial t)$ and $(\partial \hat{r}/\partial r)$. The sum of the two lines in (46) then confirms that (40) and (42) constitute a solution of (36). A similar argument confirms that (40) and (43) constitute a solution of (37). To compute t_s we note that, from the denominators on the right-hand sides of (46), the

derivatives $(\partial u/\partial t)$ and $(\partial u/\partial r)$ can become infinite if

$$\hat{t}u'_0(\hat{r}) = -1 \quad (47)$$

along one or more of the characteristics. The condition (47) is identical to (17), except that \hat{t} has replaced t . This is an important difference because, by inspection of (41), we note that $0 \leq \hat{t} < \tau$ while $0 \leq t < \infty$, i.e., the value of \hat{t} may never get large enough to satisfy (47), in which case a shock will not form. Shock formation is possible if and only if $\tau[u'_0(\hat{r}_s)] < -1$, where \hat{r}_s again denotes the characteristic that originates at the minimum value of $u'_0(r)$, i.e., $u'_0(\hat{r}_s) = [u'_0(r)]_{\min}$. In other words, if the initial radial velocity $u_0(r)$ has a large enough negative slope, the solution will become multivalued. Then, the time of shock formation, determined by combining (41) and (47), is

$$t_s = -\tau \ln \left(1 + \frac{1}{\tau u'_0(\hat{r}_s)} \right), \quad (48)$$

and the radius of shock formation, determined from (40) and (47), is

$$r_s = \hat{r}_s - \frac{u_0(\hat{r}_s)}{u'_0(\hat{r}_s)}. \quad (49)$$

Note that t_s depends on the damping time scale τ , but r_s is independent of τ and identical to that found in model I.

From the solutions for $u(r, t)$ and $v(r, t)$ we can compute the solutions for the relative vorticity $\zeta(r, t) = \partial[rv(r, t)]/r\partial r$ and the divergence $\delta(r, t) = \partial[ru(r, t)]/r\partial r$. The relative vorticity is obtained by differentiation of (43), which yields

$$\begin{aligned} \zeta(r, t) = & \left\{ \left(\frac{\frac{t}{\hat{t}} \left[1 + \left(1 - \frac{r}{\hat{r}} \right) \left(1 - \frac{2\tau(t-\hat{t})}{\hat{t}\hat{t}} \right) \right]}{1 + \hat{t}u'_0(\hat{r})} \right) f + \zeta_0(\hat{r}) \right\} \frac{\hat{r}}{r} \\ & - f \frac{t}{\hat{t}} \left[1 - \left(1 - \frac{\hat{r}}{r} \right) \left(1 - \frac{2\tau(t-\hat{t})}{\hat{t}\hat{t}} \right) \right] \right\} e^{-t/\tau}, \end{aligned} \quad (50)$$

where $\zeta_0(r) = \partial[rv_0(r)]/r\partial r$ is the initial relative vorticity. Note that (50) reduces to (20) when $(t/\tau) \ll 1$. Similarly, the boundary layer divergence, or equivalently the boundary layer pumping $w(r, t) = -h\delta(r, t)$, is obtained by using (42) in (3), which yields

$$w(r, t) = -h \left(\frac{u'_0(\hat{r})}{1 + \hat{t}u'_0(\hat{r})} + \frac{u_0(\hat{r})}{r} \right) e^{-t/\tau}. \quad (51)$$

Because of the presence of the $1 + \hat{t}u'_0(\hat{r})$ term in the denominators of both (50) and (51), the relative vorticity $\zeta(r, t)$ and the boundary layer pumping $w(r, t)$ become infinite at the same time and place.

As a simple example, again consider the initial conditions given in (22) and (23). From (48) and (49), the time and

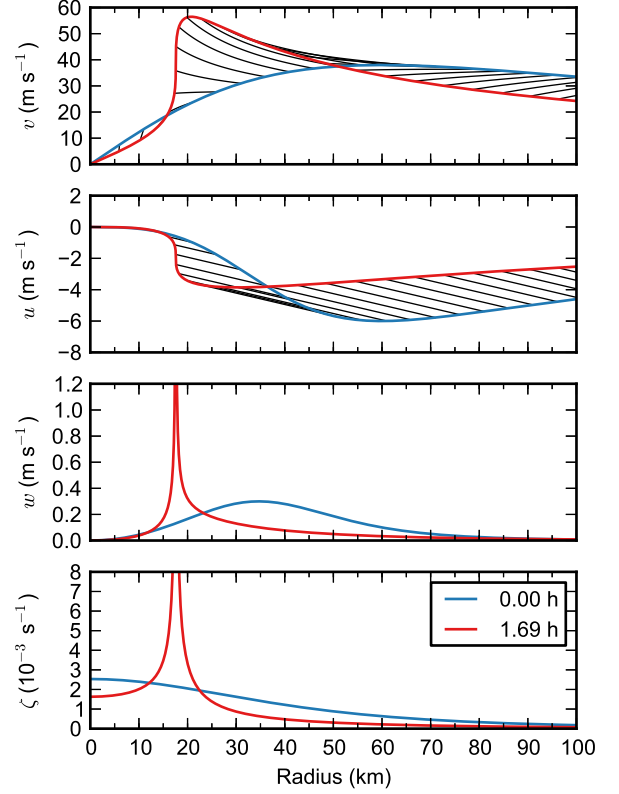


FIG. 6. The radial profiles of v, u, w, ζ at $t = 0$ (blue) and at $t = t_s = 1.69$ h (red) for analytical model II and single eyewall test case S5. Also shown by the black curves in the top two panels are fluid particle displacements for particles that are equally spaced at the initial time. At $t = t_s$ the u and v fields become discontinuous at $r = r_s = 17.6$ km, while the w and ζ fields become singular there.

radius of shock formation are

$$\begin{aligned} t_s & \approx -\tau \ln \left(1 - \frac{a}{2.032\tau|u_m|} \right), \\ r_s & \approx 0.5426 \hat{r}_s \approx 0.2931 a. \end{aligned} \quad (52)$$

The last column of Table 1 lists values of t_s obtained from model II for the seven different single eyewall test cases defined in that table. Except for the weakest vortex case (S1), all cases produce boundary layer shocks, i.e., the surface drag effects cannot prevent the development of discontinuities in the u and v fields. For the hurricane strength vortices given in Table 1, the shock formation time is generally less than 1 hour. Since $\tau = h/(c_D U)$, the top line in (52) can also be regarded as giving the shock formation time t_s as a function of the radial advection time $a/|u_m|$ and the 10 m wind speed U . Contours of t_s , as a function of $a/|u_m|$ and U are shown in Figure 4. The six dots correspond to the parameters for single eyewall test cases S2 through S7 as given in Table 1.

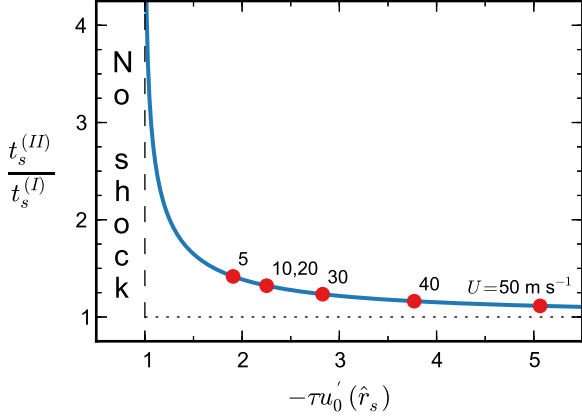


FIG. 7. The ratio of shock formation times from the two analytical models as computed from (56). The red dots correspond to the values of U given in Table 1 for the single eyewall test cases S2 through S7. Note that the dots for $U = 10 \text{ m s}^{-1}$ and for $U = 20 \text{ m s}^{-1}$ are practically colocated.

For this initial condition, the solutions (42) and (44) take the form

$$u(r, t) = u_m \left(\frac{4(\hat{r}/a)^3 e^{-t/\tau}}{1 + 3(\hat{r}/a)^4} \right), \quad (53)$$

$$rv(r, t) = \left\{ \hat{r}v_m \left(\frac{2(\hat{r}/a)}{1 + (\hat{r}/a)^2} \right) + f \frac{t}{\hat{t}} \left[\hat{r} + (r - \hat{r}) \left(\frac{\tau(t - \hat{t})}{t\hat{t}} \right) \right] (\hat{r} - r) \right\} e^{-t/\tau}, \quad (54)$$

where the characteristic curves (along which \hat{r} is fixed) are defined by

$$r = \hat{r} + u_m \hat{t} \left(\frac{4(\hat{r}/a)^3}{1 + 3(\hat{r}/a)^4} \right). \quad (55)$$

The formula for the relative vorticity can be obtained by using (25) in (50), while the formula for the boundary layer pumping can be obtained by using (22) and (24) in (51). The solutions for $u(r, t)$, $v(r, t)$, $\hat{r}(r, t)$, as given by (53)–(55), are plotted in the two panels of Figure 5 for the particular initial parameters given in Table 1 for the single eyewall test case S5 (i.e., $a = 60 \text{ km}$, $u_m = -6 \text{ m s}^{-1}$, $v_m = 38 \text{ m s}^{-1}$). The plots cover the radial interval $0 \leq r \leq 100 \text{ km}$ and the time interval $0 \leq t \leq t_s$, where $t_s = 1.69 \text{ h}$ is the shock formation time for this particular initial condition. Another view of this analytical solution is given in Figure 6, with the four panels displaying the radial profiles (at $t = 0$ in blue and at $t = t_s$ in red) of u, v, w, ζ . Also shown by the black curves in the top two panels are fluid particle displacements for particles that are equally spaced at the

initial time. At $t = t_s$ the u and v fields become discontinuous at $r = 17.6 \text{ km}$, while the w and ζ fields become singular there.

The shock formation times for models I and II are given by (18) and (48). To see how the inclusion of surface friction lengthens the shock formation time, we can take the ratio of these two formulas to obtain

$$\frac{t_s^{(II)}}{t_s^{(I)}} = \tau u'_0(\hat{r}_s) \ln \left(1 + \frac{1}{\tau u'_0(\hat{r}_s)} \right), \quad (56)$$

where the superscripts I and II have been introduced to distinguish the two models. A graph of $t_s^{(II)}/t_s^{(I)}$ as a function of $-\tau u'_0(\hat{r}_s)$ is shown in Figure 7. As noted previously, shocks do not form in model II for $-\tau u'_0(\hat{r}_s) \leq 1$. For $1 < -\tau u'_0(\hat{r}_s) < 3$ there are important differences in shock formation times from the two models, with the shock formation time lengthened by 38.6% when $-\tau u'_0(\hat{r}_s) = 2$ and by 21.6% when $-\tau u'_0(\hat{r}_s) = 3$. When $-\tau u'_0(\hat{r}_s) > 4$, the effects of surface friction do not substantially lengthen the shock formation time. For the example shown in Figures 5 and 6, $-\tau u'_0(\hat{r}_s) = 2.8$, so that the shock formation time is lengthened by 23.4% due to surface friction effects. However, it is important to note that small differences in shock formation time do not imply small differences in the

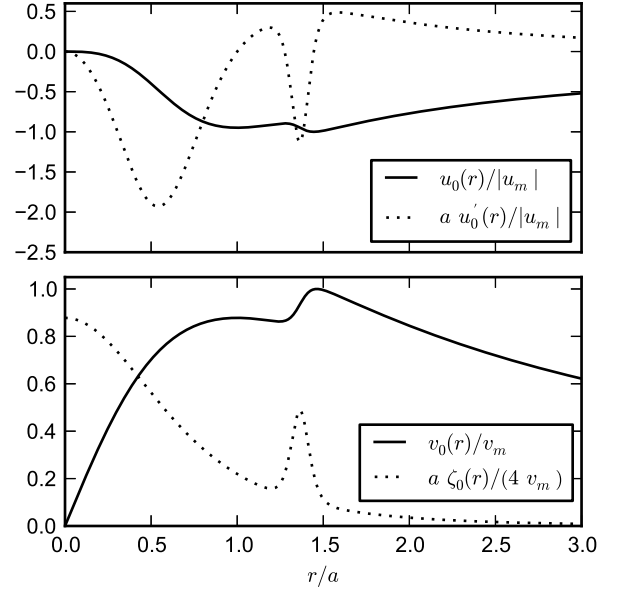


FIG. 8. The dimensionless initial conditions used in analytical model II for the double eyewall case. The solid line in the upper panel shows the dimensionless initial radial velocity $u_0(r)/|u_m|$, while the dotted line shows its dimensionless radial derivative $a u'_0(r)/|u_m|$. Similarly, the solid line in the lower panel shows the dimensionless initial tangential velocity $v_0(r)/v_m$, while the dotted line shows the dimensionless initial vorticity $a \zeta_0(r)/(4 v_m)$.

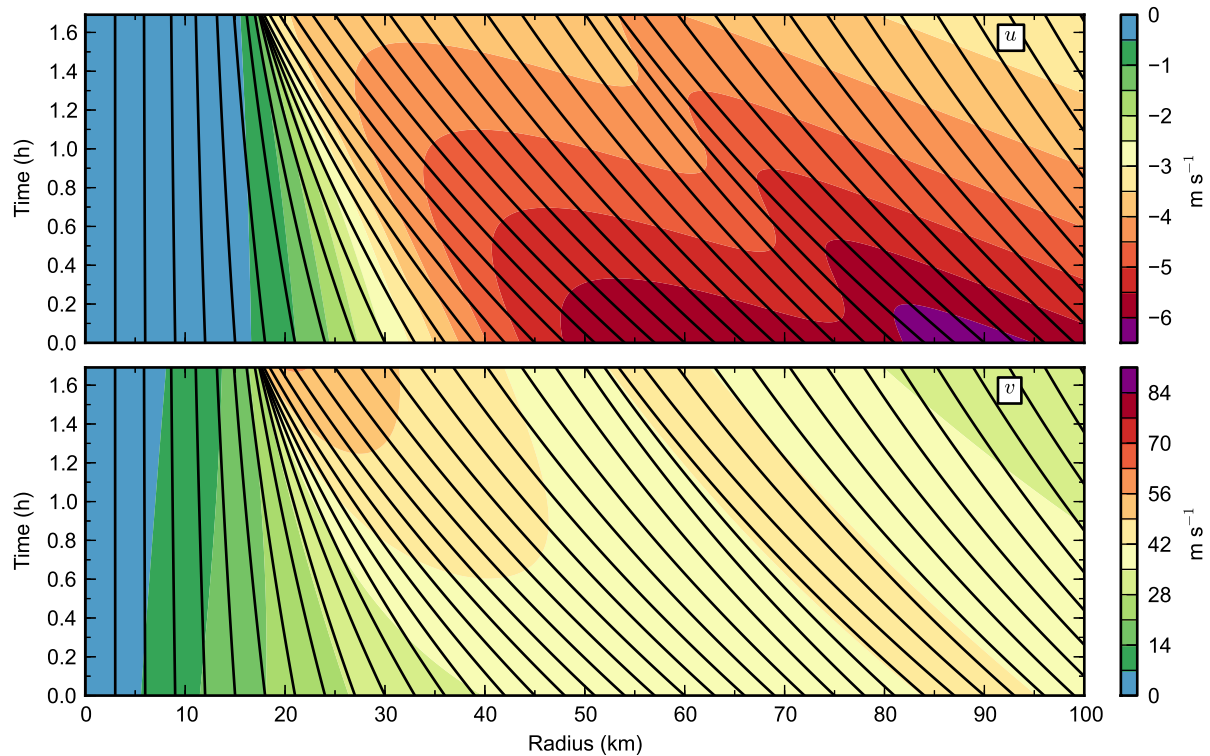


FIG. 9. The analytical solutions $u(r, t)$ and $v(r, t)$ from model II (color contours), as well as the characteristic curves (black curves on each panel), for the double eyewall case. These solutions are for the particular initial conditions shown in Figure 8, with the parameters given in Table 1 for the double eyewall test case D1 (i.e., $a = 60$ km, $u_m = -6$ m s⁻¹, $v_m = 38$ m s⁻¹). The plots cover the time interval $0 \leq t \leq t_s$, where $t_s = 1.69$ h is the shock formation time for model II with this particular initial condition.

structures of the shocks. This can be seen by comparing the red curves in the upper two panels of Figure 3 with the corresponding red curves in the upper two panels of Figure 6. For example, since the maximum tangential wind in Figure 6 is approximately 33 m s⁻¹ weaker than the maximum tangential wind in Figure 3, surface friction has played an important role in reducing the angular momentum of the inflowing boundary layer air in Figure 6.

5. Double Eyewall Case

In recent years there has been remarkable progress in our understanding of secondary eyewall formation and concentric eyewall cycles. This progress includes aircraft-based and satellite-based observational analyses (e.g., Willoughby et al. (1982), Black and Willoughby (1992), Samsury and Zipser (1995), Dodge et al. (1999), Bell et al. (2012), Hense and Houze (2012), Yang et al. (2013)), operational detection and forecasting (e.g., Willoughby and Black (1996), Maclay et al. (2008), Kossin and Sitkowski (2009, 2012), Sitkowski et al. (2011, 2012)), analytical analyses and numerical simulations using idealized models (e.g., Shapiro and Willoughby

(1982), Nong and Emanuel (2003), Kuo et al. (2004, 2008, 2009), Rozoff et al. (2006, 2008), Menelaou et al. (2013)), and, most recently, numerical simulations with three-dimensional full-physics models (e.g., Houze et al. (2007); Terwey and Montgomery (2008); Wang (2008, 2009); Zhou and Wang (2009); Judt and Chen (2010); Abarca and Corbosiero (2011); Martinez et al. (2011); Rozoff et al. (2012); Wu et al. (2012); Huang et al. (2012); Menelaou et al. (2012); Lee and Chen (2012); Chen and Zhang (2013); Wang et al. (2013); Abarca and Montgomery (2013)). These three-dimensional simulations, although run at coarser horizontal resolutions than the present axisymmetric slab model, can be interpreted as demonstrating the importance of the boundary layer shock phenomenon.

In order to better understand the formation of concentric eyewalls, we now consider solutions of analytical model II for an initial condition that leads to double shocks. In this example, the initial dimensionless radial wind $u_0(r)/|u_m|$ and its dimensionless derivative $au'_0(r)/|u_m|$ are given by the solid and dotted lines in the upper panel of Figure 8, while the initial dimension-

less tangential wind $v_0(r)/v_m$ and the initial dimensionless relative vorticity $a\zeta_0(r)/(4v_m)$ are given by the solid and dotted lines in the lower panel. Plots of $u_0(r)$, $v_0(r)$, $w_0(r)$, and $\zeta_0(r)$ in dimensional form (obtained by using the radial profiles shown in Figure 8 with the same parameters as the single eyewall test case S5) are shown by the blue curves in Figure 10. This initial condition is very similar to the initial condition shown in Figure 1, except that there are secondary peaks (just outside $r = 80$ km) in $u_0(r)$, $v_0(r)$, $w_0(r)$, and $\zeta_0(r)$. From Figure 8, note that there are two local minima in $u'_0(r)$, one at $r \approx 0.53a$ and one at $r \approx 1.36a$. Since $|u'_0(r)|$ is larger at the inner minimum, the inner shock will form before the outer shock. The analytical solutions for this example, obtained by using these initial conditions in (40), (42), (43), (50), and (51), are shown in Figures 9 and 10. As in the single eyewall case (test case S5), an inner shock develops at $r = 17.6$ km and $t = 1.69$ h. In addition, an outer shock has nearly developed by $t = 1.69$ h. Because $u_0(\hat{r}_s)/u'_0(\hat{r}_s)$

is larger for the developing outer shock, the inward radial shift ($\hat{r}_s - r_s$) predicted by (49) is larger for the developing outer shock ($\hat{r}_s - r_s \approx 31$ km) than for the inner shock ($\hat{r}_s - r_s \approx 18$ km). This model feature is consistent with the Hurricane Rita (2005) observations of Houze et al. (2007) and Didlake and Houze (2011, 2013) that show an outer eyewall with a larger outward tilt with height than the inner eyewall. It is also consistent with the structure produced in the model simulations of Zhou and Wang (2009).

One general conclusion that can be drawn from this simple solution is that double eyewalls naturally form when the radial profile of the boundary layer inflow velocity is not monotonic outside the inner eyewall. However, one unrealistic aspect of the analytic model (36)–(37) is that the radial equation of motion does not include the source term proportional to $v - v_{gr}$, so that the radial inflow simply damps along characteristics. In the more realistic numerical model results shown in section 6, this source term is included so that in subgradient regions (i.e., $v < v_{gr}$) the radial inflow can increase along characteristics.

The analytical solutions found in this section contain singularities in the boundary layer pumping $w(r, t)$ and the vorticity $\zeta(r, t)$. Obviously, such singularities do not occur in nature; their mathematical existence reflects the simplicity of the physics included in (8)–(9) and in (36)–(37). In a nonhydrostatic, full-physics hurricane model, spikes in the radial distribution of boundary layer pumping might be expected to collapse to the spatial scale of an individual cumulonimbus cloud, within which the vertical velocity would be limited by nonhydrostatic moist physics.

For the idealized analytical, double eyewall problem discussed here, the shock behavior is essentially determined by the nonzero initial condition $u_0(r)$. In the next section we set $u_0(r) = 0$ and allow the $u(r, t)$ field to develop through the $[f + (v + v_{gr})/r](v - v_{gr})$ term in (1), with v_{gr} a specified function of r .

6. Numerical Solutions for Double Eyewalls

In this section we present solutions of the problem (1)–(7), which has been solved numerically using centered, second-order spatial finite difference methods on the domain $0 \leq r \leq 1000$ km with a uniform radial grid spacing of 100 m and a fourth-order Runge-Kutta time differencing scheme with a time step of 1 s. The constants have been chosen as $h = 1000$ m, $f = 5.0 \times 10^{-5} \text{ s}^{-1}$, and $K = 1500 \text{ m}^2 \text{ s}^{-1}$. The forcing has been designed to illustrate how the boundary layer flow transitions from one quasi-steady-state to another in response to an expansion of the balanced wind and vorticity fields above the boundary layer.

Five numerical experiments have been performed. For the first three experiments, the forcing $v_{gr}(r)$ is shown in the lower panel of Figure 11, with the associated $\zeta_{gr}(r)$ shown in the upper panel. All three forcing profiles have

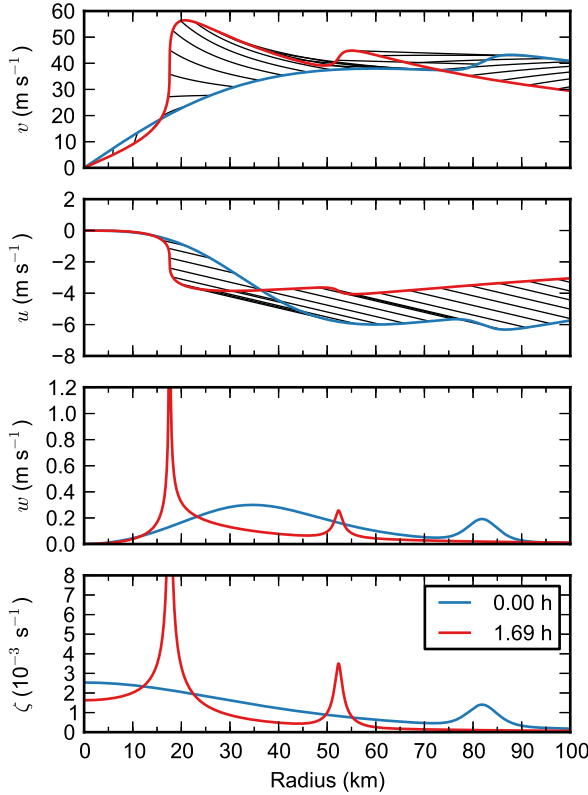


FIG. 10. The radial profiles of u, v, w, ζ at $t = 0$ (blue) and at $t = t_s = 1.69$ h (red) for analytical model II and double eyewall test case D1. Also shown by the black curves in the top two panels are fluid particle displacements for particles that are equally spaced at the initial time. At $t = t_s$ the u and v fields become discontinuous at $r = 17.6$ km, while the w and ζ fields become singular there.

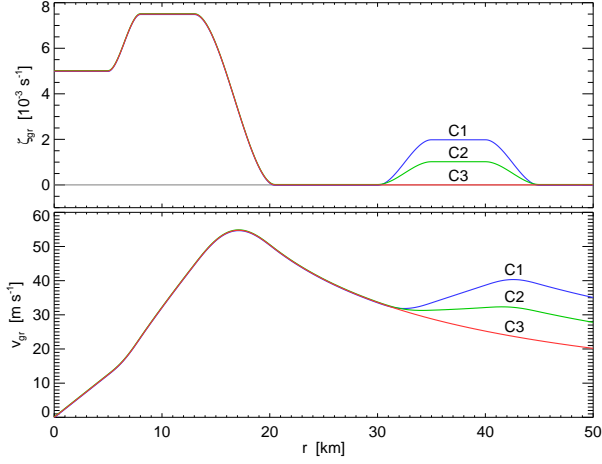


FIG. 11. Radial distribution of the forcing $v_{\text{gr}}(r)$ (bottom panel) and the associated vorticity $\zeta_{\text{gr}}(r)$ (top panel) for cases C1, C2, and C3 of the numerical model. All three forcing profiles have the same $\zeta_{\text{gr}}(r)$ and the same $v_{\text{gr}}(r)$ for $r \leq 30$ km.

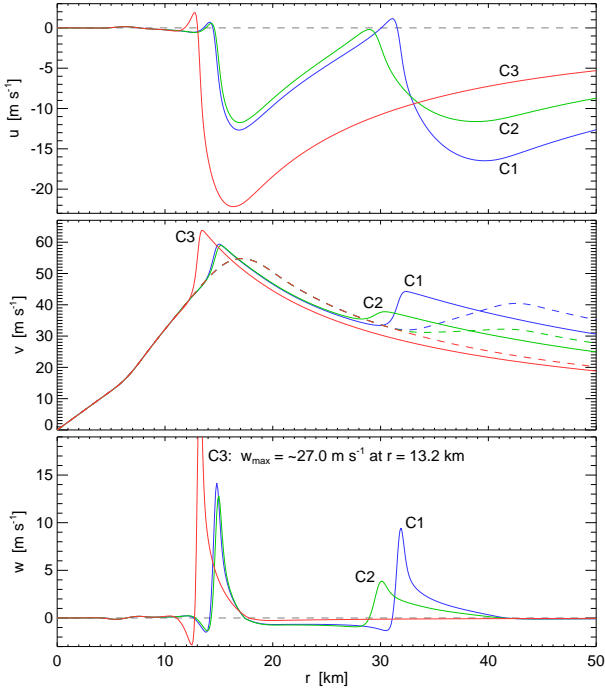


FIG. 12. Steady state slab boundary layer radial profiles of radial velocity u (top panel), tangential velocity v (middle panel), and vertical velocity w (bottom panel), for the three forcing profiles shown in Figure 11. The radial profile of w for the case with no concentric eyewall reaches a peak of 27 m s^{-1} , but has been cut off at 19 m s^{-1} for clarity of the other profiles.

the same $v_{\text{gr}}(r)$ and the same $\zeta_{\text{gr}}(r)$ for $r \leq 30$ km. For experiments C1 and C2, the $\zeta_{\text{gr}}(r)$ profiles have been locally ($30 < r < 45$ km) enhanced over that of experiment C3, so that the associated $v_{\text{gr}}(r)$ profiles differ for $r > 30$ km. One can consider the sequence $\text{C3} \rightarrow \text{C2} \rightarrow \text{C1}$ as an enhancement of the outer gradient balanced flow while the inner core balanced flow remains unchanged. For each of these three specified $v_{\text{gr}}(r)$ forcing functions, the numerical model was integrated until a steady state was obtained. Such steady states are generally obtained quickly, with most of the change from the initial conditions $u(r, 0) = 0$ and $v(r, 0) = v_{\text{gr}}(r)$ occurring in the first hour, and only small changes occurring after 3 hours. Figure 12 shows the steady state boundary layer flows beneath each of these three forcing functions. The three panels show radial profiles ($0 \leq r \leq 50$ km) of the boundary layer radial wind u (top panel), tangential wind v (middle panel), and vertical velocity w (bottom panel). Note that, for each case, strong radial inflow, supergradient/subgradient tangential winds, and large boundary layer pumping develop. Due to the $u(\partial u / \partial r)$ term in the radial equation of motion, Burgers' shock-like structures develop just inside the local maxima in the initial tangential wind. At the inner eyewall ($r \approx 16.5$ km) the maximum radial inflows are 22 m s^{-1} for case C3, 11.5 m s^{-1} for case C2, and 12.5 m s^{-1} for case C1, so the strength of the inner eyewall shock is considerably reduced by the presence of an outer shock. Note that, even though cases C1 and C2 have stronger inflow than case C3 at $r \approx 40$ km, the situation is reversed at $r \approx 30$ km, a radius at which the radial inflow has been reduced to essentially zero for cases C1 and C2. Although the radial inflows for cases C1 and C2 do somewhat recover in the moat region between the two eyewalls ($16.5 < r < 29$ km), the width of the moat and the strength of the forcing $[f + (v + v_{\text{gr}})/r](v - v_{\text{gr}})$ are not large enough to allow a full recovery of the radial inflow, leading to an inner eyewall boundary layer pumping (bottom panel of Figure 12) that is reduced to approximately 50% of the value obtained in case C3.

The forcing functions for two additional experiments, denoted as C4 and C5, are shown in Figure 13. For reference, the previously discussed case C3 is also shown. Cases C3, C4, and C5 have the same $v_{\text{gr}}(r)$ for $r > 45$ km. In the sequence $\text{C3} \rightarrow \text{C4} \rightarrow \text{C5}$, the inner eyewall vorticity decreases and the outer eyewall vorticity increases in such a way that the area averaged vorticity inside $r = 45$ km remains unchanged. The results for cases C3, C4, and C5 are shown in Figure 14. Again, the radial inflow for cases C4 and C5 is reduced to essentially zero on the inside edge of the outer shock, and now the recovery of inflow in the moat is even weaker because the values of v and v_{gr} are so nearly equal that the $(v - v_{\text{gr}})$ term in (1) is unable to reestablish significant inflow at the radius of the inner eyewall. In case C5, the result is a boundary layer pumping of less than 1

m s^{-1} at $r = 16.5$ km. Thus, by shutting off the radial inflow to the inner eyewall, the outer eyewall can take over the role of the most diabatically active region.

Barnes et al. (1983) argued that an outer spiral band or outer eyewall acts as a partial barrier, creating hostile conditions for the inner eyewall. The present results support this general line of reasoning, with added support for the idea that the partial barrier exists, not in the free troposphere, but in the frictional boundary layer. The hostile conditions for the inner eyewall result from a boundary layer shock-like feature produced at the outer eyewall. At the inner edge of this boundary layer feature, the radial inflow can be greatly reduced, and, if the moat is narrow and the tangential velocity in the moat is only weakly subgradient, the radial inflow cannot sufficiently recover to provide for the maintenance of the inner eyewall. The results presented here also support the boundary layer control arguments of Huang et al. (2012) and Abarca and Montgomery (2013), which state that a radially expanding tangential wind field above the boundary layer is necessary for secondary eyewall formation and subsequent decay of the inner eyewall.

7. Concluding Remarks

The results presented here provide some insight into questions such as: (1) What determines the size of the eye? (2) How are potential vorticity rings produced? (3) How does an outer concentric eyewall form and how does it influence the inner eyewall? The slab boundary layer results support the notion that the size of the eye is determined by

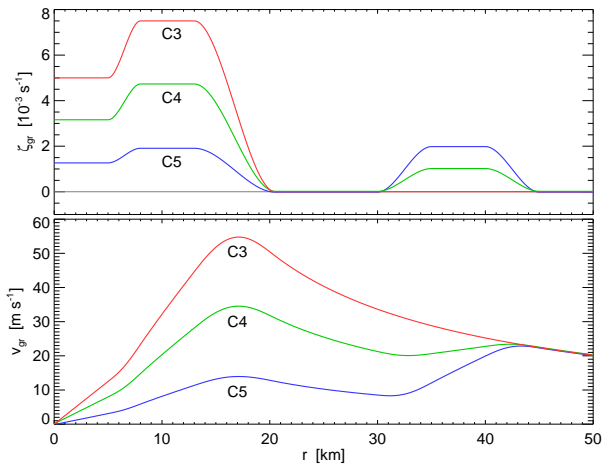


FIG. 13. Radial distribution of the forcing $v_{gr}(r)$ (bottom panel) and the associated vorticity $\zeta_{gr}(r)$ (top panel) for cases C3, C4, and C5 of the numerical model. All three forcing profiles have the same area-average vorticity inside $r = 45$ km, so the corresponding $v_{gr}(r)$ profiles are identical for $r \geq 45$ km.

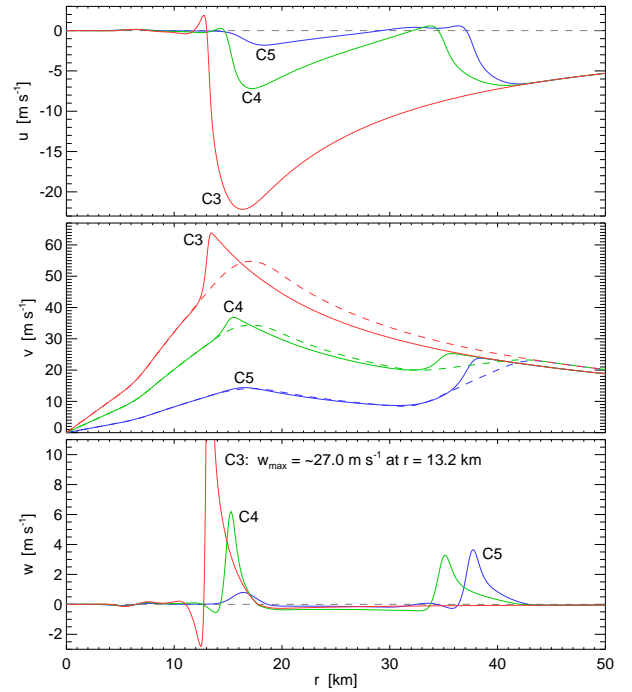


FIG. 14. Steady state slab boundary layer radial profiles of radial velocity u (top panel), tangential velocity v (middle panel), and vertical velocity w (bottom panel), for the three forcing profiles shown in Figure 13. The radial profile of w for the case with no concentric eyewall reaches a peak of 27 m s^{-1} , but has been cut off at 12 m s^{-1} for clarity of the other profiles.

nonlinear processes that set the radius at which the eyewall shock forms. A boundary layer potential vorticity ring is also produced at this radius. By boundary layer pumping and latent heat release, the boundary layer PV ring is extended upward. If, outside the eyewall, the boundary layer radial inflow does not decrease monotonically with radius, a concentric eyewall boundary layer shock can form. If it is strong enough and close enough to the inner eyewall, this outer eyewall shock can choke off the boundary layer radial inflow to the inner shock and effectively shut down the boundary layer pumping at the inner eyewall.

The results presented here also emphasize the dual role played by the surface stress terms. In the tangential equation of motion the surface stress term decelerates the tangential flow, producing subgradient flow ($v < v_{gr}$). In the radial equation of motion the $(v - v_{gr}) < 0$ term produces an inward radial flow down the pressure gradient, which is favorable for shock formation. In contrast, the surface stress term in the radial equation of motion tends to retard shock formation. For storms of hurricane intensity and with a small enough radius of maximum gradient wind, this retarding effect is overcome by the shock generation

process.

An issue that sometimes arises in the interpretation of modeling results is whether hurricane development is a top-down or a bottom-up process (Nolan 2007). One possible interpretation of the present results is that, early in the development, the process is top-down as the free-tropospheric vortex organizes and imposes a radial pressure gradient on the boundary layer. Later, as a boundary layer shock forms, the process is bottom-up, with the spike in boundary layer pumping setting the radius of the eyewall and hence the size of the eye.

Since the near-accident in Hurricane Hugo (Marks et al. 2008), research aircraft have not generally flown in the inner core boundary layer, which means that this region of strong winds tends to be undersampled, although the lack of flight level observations can be partially compensated through the use of dropsondes and remote sensing from higher flight levels. An important challenge is the development of methods to safely obtain in-situ observations in the inner core boundary layer.

We have studied only the response to axisymmetric, non-translating pressure fields with a constant depth, in which case the boundary layer shocks are circular. The problem of the boundary layer response to a translating pressure field was pioneered by Chow (1971) and Shapiro (1983). When the pressure field translates, the shocks may become spiral shaped, as has been recently discussed by Williams (2012). Also, as discussed by Kepert (2010a,b), the constant depth limits the slab boundary layer model’s ability to resolve important features of the tropical cyclone that are found in height-resolving models. Another limitation of the present study is that we have only explored the boundary layer dynamics of double eyewalls, whereas some tropical cyclones can have more than two eyewalls. A well-documented case of triple eyewalls was provided by McNoldy (2004) for Hurricane Juliette (2001), which had peaks in relative vorticity at 9, 54, and 82 km. Similar dynamical concepts should apply to the understanding of triple eyewalls, although the axisymmetry assumption is probably less valid for the outermost eyewall.

In closing it is interesting to note that there are many hints of the existence of boundary layer shocks in the observational and modeling literature on hurricanes. One of the earliest comes from the insightful observational work of Malkus (1958). In describing the structure of the mature hurricane eye, she notes that “the eye has several other mysterious features, the most striking being the weak winds within it, despite the raging cyclonic gales in the convective wall only a few kilometers away.” This description is consistent with the U-shaped tangential wind profiles that evolve during boundary layer shock formation.

APPENDIX

Characteristic Form

Equations (1)–(7) constitute a quasi-linear first order system, i.e., the system is linear in the first derivatives but the coefficients of these derivatives are functions of the dependent variables u and v . In the absence of the horizontal diffusion terms, these equations constitute a hyperbolic system, which means that it can be rewritten in characteristic form. Knowledge of the characteristic form allows for a deeper understanding of the way that characteristics can intersect and thereby produce discontinuities in u and v and singularities in w and ζ . To derive the characteristic form we shall rearrange (1) and (2) in such a way that all the terms involving the derivatives $(\partial u/\partial t)$, $(\partial u/\partial r)$, $(\partial v/\partial t)$, $(\partial v/\partial r)$ appear on the left-hand sides and all the other terms appear on the right-hand sides. This procedure requires splitting the w^- terms. In regions where $w \geq 0$, the w^- terms in (1) and (2) vanish. In regions where $w < 0$, the w^- terms do not vanish, in which case these terms need to be expressed as $(\partial u/\partial r) + (u/r)$, and then the $(\partial u/\partial r)$ parts need to be kept on to the left-hand sides of (1) and (2) while the (u/r) parts need to be brought over to the right-hand sides. This procedure is easily accomplished by noting that the mass continuity equation (3) yields

$$w^- = (1 - \alpha)h \left(\frac{\partial u}{\partial r} + \frac{u}{r} \right) \quad \text{where } \alpha = \begin{cases} 1 & \text{if } w \geq 0 \\ 0 & \text{if } w < 0, \end{cases} \quad (\text{A1})$$

which allows (1) and (2) to be written in the form

$$\frac{\partial u}{\partial t} + (2 - \alpha)u \frac{\partial u}{\partial r} = F_1, \quad (\text{A2})$$

$$\frac{\partial m}{\partial t} + u \frac{\partial m}{\partial r} + (1 - \alpha)(m - m_{\text{gr}}) \frac{\partial u}{\partial r} = F_2, \quad (\text{A3})$$

where $m_{\text{gr}} = rv_{\text{gr}} + \frac{1}{2}fr^2$ is the gradient absolute angular momentum and

$$F_1 = -\frac{(1 - \alpha)u^2}{r} + \left(f + \frac{v + v_{\text{gr}}}{r} \right) (v - v_{\text{gr}}) - c_D U \frac{u}{h}, \quad (\text{A4})$$

$$F_2 = -\frac{(1 - \alpha)u(m - m_{\text{gr}})}{r} - c_D U \frac{rv}{h}, \quad (\text{A5})$$

The forms (A2) and (A3) are convenient because the nonlinearities associated with spatial derivatives are on the left-hand side while all the other linear and nonlinear terms are on the right-hand side. The classification of the system (A2) and (A3) as a hyperbolic system and the determination of the characteristic form of this system depends on finding the eigenvalues and left eigenvectors of the matrix A , which is defined by

$$A = \begin{pmatrix} (2 - \alpha)u & 0 \\ (1 - \alpha)(m - m_{\text{gr}}) & u \end{pmatrix} \quad (\text{A6})$$

(see Chapter 5 of Whitham (1974)). Note that the matrix A is composed of the coefficients of the $(\partial u/\partial r)$ and

$(\partial m / \partial r)$ terms on the left-hand sides of (A2) and (A3). For $n = 1, 2$, let $\begin{pmatrix} \ell_1^{(n)} & \ell_2^{(n)} \end{pmatrix}$ be the left eigenvector of A corresponding to the eigenvalue $\lambda^{(n)}$, i.e.,

$$\begin{pmatrix} \ell_1^{(n)} & \ell_2^{(n)} \end{pmatrix} \begin{pmatrix} (2 - \alpha)u & 0 \\ (1 - \alpha)(m - m_{\text{gr}}) & u \end{pmatrix} = \lambda^{(n)} \begin{pmatrix} \ell_1^{(n)} & \ell_2^{(n)} \end{pmatrix}. \quad (\text{A7})$$

As is easily checked by direct substitution into (A7), the two eigenvalues and the two corresponding left eigenvectors are

$$\begin{aligned} \lambda^{(1)} = (2 - \alpha)u &\iff \ell_1^{(1)} = 1, \ell_2^{(1)} = 0, \\ \lambda^{(2)} = u &\iff \ell_1^{(2)} = m - m_{\text{gr}}, \ell_2^{(2)} = -u. \end{aligned} \quad (\text{A8})$$

Since the eigenvalues $\lambda^{(1)}$ and $\lambda^{(2)}$ are real and the corresponding left eigenvectors are linearly independent, the system (A2)–(A3) is hyperbolic and can be rewritten in characteristic form. To obtain this characteristic form, we next take the sum of $\ell_1^{(n)}$ times (A2) and $\ell_2^{(n)}$ times (A3) to obtain

$$\begin{aligned} \ell_1^{(n)} \left\{ \frac{\partial u}{\partial t} + \left[(2 - \alpha)u + (1 - \alpha)(m - m_{\text{gr}}) \frac{\ell_2^{(n)}}{\ell_1^{(n)}} \right] \frac{\partial u}{\partial r} \right\} \\ + \ell_2^{(n)} \left\{ \frac{\partial m}{\partial t} + u \frac{\partial m}{\partial r} \right\} = \ell_1^{(n)} F_1 + \ell_2^{(n)} F_2. \end{aligned} \quad (\text{A9})$$

Using the eigenvector components given in (A8), equation (A9) becomes (for $n = 1$ and $n = 2$)

$$\frac{\partial u}{\partial t} + (2 - \alpha)u \frac{\partial u}{\partial r} = F_1, \quad (\text{A10})$$

$$(m - m_{\text{gr}}) \left(\frac{\partial u}{\partial t} + u \frac{\partial u}{\partial r} \right) - u \left(\frac{\partial m}{\partial t} + u \frac{\partial m}{\partial r} \right) = F_3, \quad (\text{A11})$$

where

$$\begin{aligned} F_3 &= (m - m_{\text{gr}})F_1 - uF_2 \\ &= \left(f + \frac{v + v_{\text{gr}}}{r} \right) r (v - v_{\text{gr}})^2 + \frac{c_D U u r v_{\text{gr}}}{h}. \end{aligned} \quad (\text{A12})$$

Since (A10) is identical to (A2), we conclude that (A2) is already in characteristic form. We now write (A10) and (A11) in the form

$$\frac{du}{dt} = F_1 \quad \text{on} \quad \frac{dr}{dt} = (2 - \alpha)u, \quad (\text{A13})$$

$$(m - m_{\text{gr}}) \frac{du}{dt} - u \frac{dm}{dt} = F_3 \quad \text{on} \quad \frac{dr}{dt} = u. \quad (\text{A14})$$

Equations (A13) and (A14) constitute the characteristic form of the original system (A2) and (A3). An advantage of (A13) and (A14) is that, along each family of characteristic curves, the partial differential equations have been reduced to ordinary differential equations. It is interesting

to note that, in regions of subsidence (i.e., where $\alpha = 0$), information on u is carried along characteristics given by $(dr/dt) = 2u$, while information on a combination of u and m is carried along characteristics given by $(dr/dt) = u$. Thus, in regions of subsidence there are two distinct families of characteristics. In contrast, for regions of boundary layer pumping (i.e., where $\alpha = 1$), the two families of characteristics become identical.

Although in practice the forcing terms F_1 and F_3 are too complicated to allow analytical solution of (A13) and (A14), the numerical solution of these ordinary differential equations can serve as the basis of the shock-capturing methods described by LeVeque (2002). In section 6 we have adopted the simpler approach of solving (1)–(7) using standard finite differences with the inclusion of horizontal diffusion to control the solution near shocks. Although this approach has some disadvantages (e.g., unphysical oscillation near a shock), it provides a useful guide to the expected results when full-physics hurricane models can be run at the high horizontal resolution used here.

In regions where $w < 0$, we have $\alpha = 0$ and the characteristic forms (A13) and (A14) distinguish two families of characteristics, one given by $(dr/dt) = 2u$ and one given by $(dr/dt) = u$. In regions where $w \geq 0$, we have $\alpha = 1$ and there is only one family of characteristics, given by $(dr/dt) = u$. In that case, (A13) can be used to eliminate (du/dt) in (A14), which leads to the conclusion that $(du/dt) = F_1$ and $(dm/dt) = F_2$ on $(dr/dt) = u$. This case of only one family of characteristics is the one explored analytically in sections 3 and 4, with the forcing terms F_1 and F_2 set to zero in section 3, and with these forcing terms representing linear surface drag in section 4.

In passing we note that there is a less formal, more intuitive route from (A2) and (A3) to the characteristic forms (A13) and (A14). This intuitive route results from simply noting that (A2) is already in characteristic form and can be directly written as (A13), while the characteristic form (A14) can be simply obtained by combining (A2) and (A3) in such a way as to eliminate terms containing the factor $(1 - \alpha)(\partial u / \partial r)$.

Acknowledgments.

We would like to thank Joseph Biello, Paul Ciesielski, Mark DeMaria, Alex Gonzalez, Hung-Chi Kuo, and Hugh Willoughby for their comments. This research has been supported by the Hurricane Forecast Improvement Project (HFIP) through the Department of Commerce (DOC) National Oceanic and Atmospheric Administration (NOAA) Grant NA090AR4320074 and through the National Science Foundation under Grants ATM-0837932 and AGS-1250966 and under the Science and Technology Center for Multi-Scale Modeling of Atmospheric Processes, managed by Colorado State University through cooperative agreement No. ATM-0425247. The calculations were made on high-end

Linux workstations generously provided through a gift from the Hewlett-Packard Corporation. This manuscript was generated using a modified version of the American Meteorological Society L^AT_EX template for journal page layout.

REFERENCES

- Abarca, S. F., and K. L. Corbosiero, 2011: Secondary eyewall formation in WRF simulations of Hurricanes Rita and Katrina (2005). *Geophys. Res. Lett.*, **38**, L07802.
- Abarca, S. F., and M. T. Montgomery, 2013: Essential dynamics of secondary eyewall formation. *J. Atmos. Sci.*, **70**, 3216–3230.
- Barnes, G. M., E. J. Zipser, D. Jorgensen, and F. Marks, 1983: Mesoscale and convective structure of a hurricane rainband. *J. Atmos. Sci.*, **40**, 2125–2137.
- Bell, M. M., M. T. Montgomery, and W.-C. Lee, 2012: An axisymmetric view of concentric eyewall evolution in Hurricane Rita (2005). *J. Atmos. Sci.*, **69**, 2414–2432.
- Black, M. L., and H. E. Willoughby, 1992: The concentric eyewall cycle of Hurricane Gilbert. *Mon. Wea. Rev.*, **120**, 947–957.
- Chen, H., and D.-L. Zhang, 2013: On the rapid intensification of Hurricane Wilma (2005), Part II: Convective bursts and the upper-level warm core. *J. Atmos. Sci.*, **70**, 146–172.
- Chow, S., 1971: A study of the wind field in the planetary boundary layer of a moving tropical cyclone. M.S. thesis, Dept. of Meteorology and Oceanography, New York University, 59 pp.
- Didlake, A. C., and R. A. Houze, 2011: Kinematics of the secondary eyewall observed in Hurricane Rita (2005). *J. Atmos. Sci.*, **68**, 1620–1636.
- Didlake, A. C., and R. A. Houze, 2013: Convective-scale variations in the inner-core rainbands of a tropical cyclone. *J. Atmos. Sci.*, **70**, 504–523.
- Dodge, P., R. W. Burpee, and F. D. M. Jr., 1999: The kinematic structure of a hurricane with sea level pressure less than 900 mb. *Mon. Wea. Rev.*, **127**, 987–1004.
- Durran, D. R., 2010: *Numerical Methods for Fluid Dynamics*, Texts in Applied Mathematics, Vol. 32. 2nd ed., Springer, 516 pp.
- Emanuel, K. A., 1986: An air-sea interaction theory for tropical cyclones, Part I: Steady-state maintenance. *J. Atmos. Sci.*, **43**, 585–605.
- Emanuel, K. A., 1989: The finite-amplitude nature of tropical cyclogenesis. *J. Atmos. Sci.*, **46**, 3431–3456.
- Hausman, S. A., K. V. Ooyama, and W. H. Schubert, 2006: Potential vorticity structure of simulated hurricanes. *J. Atmos. Sci.*, **63**, 87–108.
- Hence, D. A., and R. A. Houze, 2012: Vertical structure of tropical cyclones with concentric eyewalls as seen by the TRMM precipitation radar. *J. Atmos. Sci.*, **69**, 1021–1036.
- Houze, R. A., S. Chen, B. F. Smull, W.-C. Lee, and M. M. Bell, 2007: Hurricane intensity and eyewall replacement. *Science*, **315**, 1235–1239.
- Huang, Y.-H., M. T. Montgomery, and C.-C. Wu, 2012: Concentric eyewall formation in Typhoon Sinlaku (2008). Part II: Axisymmetric dynamical processes. *J. Atmos. Sci.*, **69**, 662–674.
- Judt, F., and S. S. Chen, 2010: Convectively generated potential vorticity in rainbands and formation of the secondary eyewall in Hurricane Rita of 2005. *J. Atmos. Sci.*, **67**, 3581–3599.
- Kepert, J. D., 2001: The dynamics of boundary layer jets within the tropical cyclone core. Part I: Linear theory. *J. Atmos. Sci.*, **58**, 2469–2484.
- Kepert, J. D., 2010a: Comparing slab and height-resolving models of the tropical cyclone boundary layer. Part I: Comparing the simulations. *Quart. J. Roy. Meteor. Soc.*, **136**, 1689–1699.
- Kepert, J. D., 2010b: Comparing slab and height-resolving models of the tropical cyclone boundary layer. Part I: Why the simulations differ. *Quart. J. Roy. Meteor. Soc.*, **136**, 1700–1711.
- Kepert, J. D., 2013: How does the boundary layer contribute to eyewall replacement cycles in axisymmetric tropical cyclones? *J. Atmos. Sci.*, **70**, 2808–2830.
- Kepert, J. D., and Y. Wang, 2001: The dynamics of boundary layer jets within the tropical cyclone core. Part II: Nonlinear enhancement. *J. Atmos. Sci.*, **58**, 2485–2501.
- Kossin, J. P., and M. Sitkowski, 2009: An objective model for identifying secondary eyewall formation in hurricanes. *Mon. Wea. Rev.*, **137**, 876–892.
- Kossin, J. P., and M. Sitkowski, 2012: Predicting hurricane intensity and structure changes associated with eyewall replacement cycles. *Mon. Wea. Rev.*, **27**, 484–488.
- Kuo, H.-C., C. P. Chang, Y.-T. Yang, and H.-J. Jiang, 2009: Western north pacific typhoons with concentric eyewalls. *Mon. Wea. Rev.*, **137**, 3758–3770.
- Kuo, H.-C., L. Y. Lin, C. P. Chang, and R. T. Williams, 2004: The formation of concentric vorticity structures in typhoons. *J. Atmos. Sci.*, **61**, 2722–2734.

- Kuo, H.-C., W. H. Schubert, C.-L. Tsai, and Y.-F. Kuo, 2008: Vortex interactions and barotropic aspects of concentric eyewall formation. *Mon. Wea. Rev.*, **136**, 5183–5198.
- Lee, C.-Y., and S. S. Chen, 2012: Symmetric and asymmetric structures of hurricane boundary layer in coupled atmosphere-wave-ocean models and observations. *J. Atmos. Sci.*, **69**, 3576–3594.
- LeVeque, R. J., 2002: *Finite Volume Methods for Hyperbolic Problems*. Cambridge University Press, 558 pp.
- Maclay, K. S., M. DeMaria, and T. H. V. Haar, 2008: Tropical cyclone inner-core kinetic energy evolution. *Mon. Wea. Rev.*, **136**, 4882–4898.
- Malkus, J. S., 1958: On the structure and maintenance of the mature hurricane eye. *J. Meteor.*, **15**, 337–349.
- Marks, F. D., P. G. Black, M. T. Montgomery, and R. W. Burpee, 2008: Structure of the eye and eyewall of Hurricane Hugo (1989). *Mon. Wea. Rev.*, **136**, 1237–1259.
- Martinez, Y., G. Brunet, M. K. Yau, and X. Wang, 2011: On the dynamics of concentric eyewall genesis: Space-time empirical normal modes diagnosis. *J. Atmos. Sci.*, **68**, 457–476.
- McNoldy, B. D., 2004: Triple eyewall in Hurricane Juliette. *Bull. Amer. Meteor. Soc.*, **85**, 1663–1666.
- Menelaou, K., M. K. Yau, and Y. Martinez, 2012: On the dynamics of the secondary eyewall genesis in Hurricane Wilma (2005). *Geophys. Res. Lett.*, **39**, L04801.
- Menelaou, K., M. K. Yau, and Y. Martinez, 2013: Impact of asymmetric dynamical processes on the structure and intensity change of two-dimensional hurricane-like annular vortices. *J. Atmos. Sci.*, **70**, 559–582.
- Nolan, D. S., 2007: What is the trigger for tropical cyclogenesis? *Aust. Meteor. Mag.*, **56**, 241–266.
- Nong, S., and K. A. Emanuel, 2003: A numerical study of the genesis of concentric eyewalls in hurricanes. *Quart. J. Roy. Meteor. Soc.*, **129**, 3323–3338.
- Ooyama, K., 1969a: Numerical simulation of the life cycle of tropical cyclones. *J. Atmos. Sci.*, **26**, 3–40.
- Ooyama, K., 1969b: Numerical simulation of tropical cyclones with an axi-symmetric model. *Proc. of the WMO/IUGG Symposium on Numerical Weather Prediction in Tokyo (November 26–December 4, 1968)*, Tokyo, Japan, World Meteorological Organization/International Union of Geodesy and Geophysics, 81–88.
- Rozoff, C. M., D. S. Nolan, J. P. Kossin, F. Zhang, and J. Fang, 2012: The roles of an expanding wind field and inertial stability in tropical cyclone secondary eyewall formation. *J. Atmos. Sci.*, **69**, 2621–2643.
- Rozoff, C. M., W. H. Schubert, and J. P. Kossin, 2008: Some dynamical aspects of tropical cyclone concentric eyewalls. *Quart. J. Roy. Meteor. Soc.*, **134**, 583–593.
- Rozoff, C. M., W. H. Schubert, B. D. McNoldy, and J. P. Kossin, 2006: Rapid filamentation zones in intense tropical cyclones. *J. Atmos. Sci.*, **63**, 325–340.
- Samsury, C. E., and E. J. Zipser, 1995: Secondary wind maxima in hurricanes: Airflow and relationship to rainbands. *Mon. Wea. Rev.*, **123**, 3502–3517.
- Schubert, W. H., C. M. Rozoff, J. L. Vigh, B. D. McNoldy, and J. P. Kossin, 2007: On the distribution of subsidence in the hurricane eye. *Quart. J. Roy. Meteor. Soc.*, **133**, 595–605.
- Shapiro, L. J., 1983: The asymmetric boundary layer flow under a translating hurricane. *J. Atmos. Sci.*, **40**, 1984–1998.
- Shapiro, L. J., and H. E. Willoughby, 1982: The response of balanced hurricanes to local sources of heat and momentum. *J. Atmos. Sci.*, **39**, 378–394.
- Shu, C.-W., 1998: Essentially non-oscillatory and weighted essentially non-oscillatory schemes for hyperbolic conservation laws. *Advanced Numerical Approximation of Nonlinear Hyperbolic Equations*, A. Quarteroni, Ed., No. 1697, Lecture Notes in Mathematics, Springer, 325–432.
- Sitkowski, M., J. P. Kossin, and C. M. Rozoff, 2011: Intensity and structure changes during hurricane eyewall replacement cycles. *Mon. Wea. Rev.*, **139**, 3829–3847.
- Sitkowski, M., J. P. Kossin, C. M. Rozoff, and J. A. Knaff, 2012: Hurricane eyewall replacement cycle thermodynamics and the relict inner eyewall circulation. *Mon. Wea. Rev.*, **140**, 4035–4045.
- Slocum, C. J., 2013: Diabatic and frictional forcing effects on the structure and intensity of tropical cyclones. M.S. thesis, Dept. of Atmos. Sci. Colorado State University, 77 pp.
- Smith, R. K., 2003: A simple model of the hurricane boundary layer. *Quart. J. Roy. Meteor. Soc.*, **129**, 1007–1027.
- Smith, R. K., and M. T. Montgomery, 2008: Balanced boundary layers in hurricane models. *Quart. J. Roy. Meteor. Soc.*, **134**, 1385–1395.

- Smith, R. K., and M. T. Montgomery, 2010: Hurricane boundary-layer theory. *Quart. J. Roy. Meteor. Soc.*, **136**, 1665–1670.
- Smith, R. K., M. T. Montgomery, and S. V. Nguyen, 2009: Tropical cyclone spin-up revisited. *Quart. J. Roy. Meteor. Soc.*, **135**, 1321–1335.
- Smith, R. K., M. T. Montgomery, and S. Vogl, 2008: A critique of emmanuel’s hurricane model and potential intensity theory. *Quart. J. Roy. Meteor. Soc.*, **134**, 551–561.
- Smith, R. K., and G. L. Thomsen, 2010: Dependence of tropical-cyclone intensification on the boundary-layer representation in a numerical model. *Quart. J. Roy. Meteor. Soc.*, **136**, 1670–1685.
- Smith, R. K., and S. Vogl, 2008: A simple model of the hurricane boundary layer revisited. *Quart. J. Roy. Meteor. Soc.*, **134**, 337–351.
- Terwey, W. D., and M. T. Montgomery, 2008: Secondary eyewall formation in two idealized, full-physics modeled hurricanes. *J. Geophys. Res.*, **113**, D12 112.
- Wang, X., 2008: Rapid filamentation zone in a numerically simulated tropical cyclone. *J. Atmos. Sci.*, **65**, 1158–1181.
- Wang, X., 2009: How do outer spiral rainbands affect tropical cyclone structure and intensity? *J. Atmos. Sci.*, **66**, 1250–1273.
- Wang, X., Y. Ma, and N. E. Davidson, 2013: Secondary eyewall formation and eyewall replacement cycles in a simulated hurricane: Effect of the net radial force in the hurricane boundary layer. *J. Atmos. Sci.*, **70**, 1317–1341.
- Whitham, G. B., 1974: *Linear and Nonlinear Waves*. John Wiley and Sons, 363 pp.
- Williams, G. J., 2012: The effects of environmental flow on the internal asymmetric dynamics of tropical cyclones. Ph.D. thesis, Colorado State University, 185 pp.
- Williams, G. J., R. K. Taft, B. D. McNoldy, and W. H. Schubert, 2013: Shock-like structures in the tropical cyclone boundary layer. *J. Adv. Model. Earth Syst.*, **5**, 338–353.
- Willoughby, H. E., and P. G. Black, 1996: Hurricane Andrew in Florida: Dynamics of a disaster. *Bull. Amer. Meteor. Soc.*, **77**, 543–549.
- Willoughby, H. E., J. A. Clos, and M. G. Shoreibah, 1982: Concentric eye walls, secondary wind maxima, and the evolution of the hurricane vortex. *J. Atmos. Sci.*, **39**, 395–411.
- Wu, C.-C., Y.-H. Huang, and G.-Y. Lien, 2012: Concentric eyewall formation in Typhoon Sinlaku (2008). Part I: Assimilation of T-PARC data based on the ensemble Kalman filter (EnKF). *Mon. Wea. Rev.*, **140**, 506–527.
- Yamasaki, M., 1983: A further study of the tropical cyclone without parameterizing the effects of cumulus convection. *Pap. Meteor. Geophys.*, **34**, 221–260.
- Yang, Y.-T., H.-C. Kuo, E. A. Hendricks, and M. S. Peng, 2013: Structural and intensity changes of concentric eyewall typhoons in the western north pacific basin. *Mon. Wea. Rev.*, **141**, 2632–2648.
- Zhou, X., and B. Wang, 2009: From concentric eyewall to annular hurricane: A numerical study with the cloud-resolved WRF model. *Geophys. Res. Lett.*, **36**, L03 802.